Multiscale reactor modelling of total pressure effects on complete methane oxidation over Pd/Al2O3

Downloaded from: https://research.chalmers.se, 2021-08-31 15:53 UTC

Citation for the original published paper (version of record):
Florén, C., Carlsson, P., Creaser, D. et al (2019)
Multiscale reactor modelling of total pressure effects on complete methane oxidation over Pd/Al2O3
Catalysis Science and Technology, 9(12): 3055-3065
http://dx.doi.org/10.1039/c8cy02461h

N.B. When citing this work, cite the original published paper.

research.chalmers.se offers the possibility of retrieving research publications produced at Chalmers University of Technology.
It covers all kind of research output: articles, dissertations, conference papers, reports etc. since 2004.
research.chalmers.se is administrated and maintained by Chalmers Library

(article starts on next page)

Catalysis Science & Technology

PAPER

View Article Online
View Journal | View Issue

Check for updates

Cite this: *Catal. Sci. Technol.*, 2019, 9, 3055

Multiscale reactor modelling of total pressure effects on complete methane oxidation over Pd/Al_2O_3†

Carl-Robert Florén, *[a] Per-Anders Carlsson, [a] Derek Creaser,[a] Henrik Grönbeck[b] and Magnus Skoglundh [a]

A two-dimensional multiscale model is developed for complete methane oxidation in a continuous flow reactor. The model considers mass and heat transfer for a porous alumina supported palladium catalyst coated on a ceramic monolith substrate and the surface kinetics are described by a first-principles microkinetic model for complete methane oxidation over PdO(101). The temperature dependent conversion for a synthetic exhaust gas composition shows a delayed ignition but a higher conversion at elevated temperatures when the total pressure is increased from 1 to 10 atm. The simulations reveal a temperature and total pressure dependent operating point where the methane conversion is maximized. Analysis of the kinetics shows that the reaction is suppressed by bicarbonates, hydroxyl species and water originating from adsorbed carbon dioxide and water from the gas phase. The reaction order with respect to water and carbon dioxide at 1 atm is −0.94 and −0.99, respectively, and decreases with increasing total pressure. The developed model paves the way for exploring how design parameters and reaction conditions influence the complete methane oxidation reaction.

Received 5th December 2018,
Accepted 12th May 2019

DOI: 10.1039/c8cy02461h

rsc.li/catalysis

This article is licensed under a Creative Commons Attribution 3.0 Unported Licence.

1 Introduction

Natural gas is used for heat and power generation and has received increasing interest in the transportation sector.[1,2] Natural gas consists primarily of methane and is combusted with lower levels of nitrogen oxides, sulfur oxides and particulate matter compared to diesel and gasoline.[3] Methane is the main component also in biogas which can be produced by gasification or fermentation of bioorganic waste or by-products and later be upgraded using scrubbers to remove hydrogen sulfide, carbon dioxide and moisture. After upgrading, the composition of biomethane is similar to the composition of natural gas and can be used in the natural gas infrastructure.[4–7] The increased use of natural and biogas requires improved after treatment technologies since methane is a potent greenhouse gas. It is essential that uncombusted methane is removed before the exhaust is released into the atmosphere.[8] Methane combustion is generally performed over supported palladium based catalysts.[9–12] Under lean conditions, palladium oxide is reported to be the active phase and PdO(101) has been identified as the most reactive surface for methane dissociation due to the presence of undercoordinated Pd sites.[13–16]

The possibilities of modelling atomistic behaviour have increased immensely during the last few decades thanks to the large computational power. As a result, computational fluid dynamics and first-principles based models have become more common to describe fluid motion and reaction kinetics, respectively. The kinetic models can be used to describe the reactions in detail and pinpoint bottlenecks for the reaction, allowing the use of a comprehensive optimisation approach for developing high-performance materials and catalytic systems.

The present study aims to develop a multiscale reactor model for complete oxidation of methane over a supported palladium oxide catalyst where the surface reactions are described by first-principles calculations. The reactor geometry is presented as a monolithic flow reactor with porous aluminium oxide supported palladium using a single-channel monolith model. The interactions with the active palladium oxide sites are described by first-principles kinetics, and mass and heat transport effects in the porous catalyst are included in the model.

[a] *Competence Centre for Catalysis, Department of Chemistry and Chemical Engineering, Chalmers University of Technology, SE-41296 Göteborg, Sweden. E-mail: carl-robert.floren@chalmers.se*
[b] *Competence Centre for Catalysis, Department of Physics, Chalmers University of Technology, SE-41296 Göteborg, Sweden*

† Electronic supplementary information (ESI) available: Knudsen diffusion affected conversion plots and evaluation of mass transport effects on the reaction rate of complete methane oxidation. See DOI: 10.1039/c8cy02461h

This article is licensed under a Creative Commons Attribution 3.0 Unported Licence.

2 Materials and methods

2.1. Reactor model

The reactor model is based on a model in a previous study where first-principles kinetics are coupled to mass and heat transport in a porous catalyst layer.[17] The model has been extended to a two-dimensional (2D) monolith reactor model to include axial variations. The monolith is simulated as a single-channel reactor model, which has been successfully used in the past.[18,19] The channel geometry represents a monolith with 400 cpsi. The single-channel monolith is discretised into 10 tanks-in-series while the porous catalyst is divided into 12 layers to account for internal mass and heat transport axially and radially. The length of the tanks and the thickness of the layers increase successively with 30% from the inlet and 50% from the catalyst surface, respectively. In this way a finer resolution is obtained where the gradients are steeper. An illustration of the single-channel reactor is shown in Fig. 1. The chosen number of tanks and layers provides a satisfactory accuracy within a reasonable computational time. The density of the active sites is calculated, maintaining the total palladium loading in each tank and layer, to obtain an even distribution in the coated monolith substrate.

The mass balance for the bulk gas phase for component i is described by eqn (1)

$$\frac{F_{\mathrm{tot}}}{A_{\mathrm{c}}}\cdot\frac{\mathrm{d}y_{\mathrm{i,g}}}{\mathrm{d}x}-a\cdot k_{\mathrm{c,i}}\cdot C_{\mathrm{tot}}\cdot\left(y_{\mathrm{i,g}}-y_{\mathrm{i,s}}\right)=0 \tag{1}$$

where F_{tot} is the total bulk molar flow rate, A_{c} is the cross sectional area of the porous catalyst, a is the ratio of the channel surface area to the channel volume, $k_{\mathrm{c,i}}$ is the mass transport coefficient of component i and C_{tot} is the total gas phase concentration for the bulk gas. $y_{\mathrm{i,g}}$ and $y_{\mathrm{i,s}}$ are the mole fractions of component i in the bulk gas and at the porous catalyst surface, respectively. The governing heat transport equation in the axial direction is

$$\frac{F_{\mathrm{tot}}C_{\mathrm{p}}}{A_{\mathrm{c}}}\cdot\frac{\mathrm{d}T_{\mathrm{g}}}{\mathrm{d}x}-h_{\mathrm{k}}\cdot a\cdot\left(T_{\mathrm{g}}-T_{\mathrm{s}}\right)=0 \tag{2}$$

where C_{p} is the heat capacity of the bulk gas, T_{g} is the bulk gas temperature, T_{s} is the catalyst surface temperature and h_{k} is the heat transport coefficient.

The mass balance for component i inside the porous catalyst is described by eqn (3).

$$D_{\mathrm{eff,i}}\cdot C_{\mathrm{tot}}\cdot\frac{\mathrm{d}^2y_{\mathrm{i}}}{\mathrm{d}z^2}+\nu_{\mathrm{i}}\cdot C_{\mathrm{site}}\cdot\rho_{\mathrm{cat}}\cdot r\left(C_{\mathrm{s}},T_{\mathrm{s}}\right)=0 \tag{3}$$

with boundary conditions as follows

$$k_{\mathrm{c,i}}\cdot C_{\mathrm{tot}}\cdot\left(y_{\mathrm{i,g}}-y_{\mathrm{i,s}}\right)=D_{\mathrm{eff,i}}\cdot C_{\mathrm{tot}}\cdot\left.\frac{\mathrm{d}y_{\mathrm{i}}}{\mathrm{d}z}\right|_{z=0} \tag{4}$$

$$0=\left.\frac{\mathrm{d}y_{\mathrm{i}}}{\mathrm{d}z}\right|_{z=L_{\mathrm{wc}}} \tag{5}$$

where $D_{\mathrm{eff,i}}$ is the effective diffusivity and ν_{i} is the stoichiometric coefficient for component i, C_{site} is the active site density, ρ_{cat} is the density of the porous catalyst, r is the reaction rate determined from first-principles based microkinetics and L_{wc} is the thickness of the porous catalyst. No mass transport proceeds between the porous catalyst and the cordierite substrate, hence the derivative is set to zero at $z = L_{\mathrm{wc}}$ in eqn (5). In accordance to Anderson's criterion,[20] the porous catalyst is assumed to be isothermal in the radial direction. Thus, the generated heat from the exothermic oxidation reaction is transported from the catalyst surface at a temperature of T_{s} to the bulk gas phase at a temperature of T_{g}, or conducted axially through the solid material. The heat balance of the porous catalyst is described by eqn (6)

$$h_{\mathrm{k}}\cdot A_{\mathrm{s}}\cdot\left(T_{\mathrm{g}}-T_{\mathrm{s}}\right)-\left(-2\lambda_{\mathrm{s}}\right)\cdot A_{\mathrm{cs}}\cdot\frac{\mathrm{d}T_{\mathrm{s}}}{\mathrm{d}x}+\frac{\int_{z=0}^{z=L_{\mathrm{wc}}}\rho_{\mathrm{cat}}\cdot C_{\mathrm{site}}\cdot\left(-\Delta H_{\mathrm{r}}\right)\cdot r\left(C_{\mathrm{s}},T_{\mathrm{s}}\right)\cdot\mathrm{d}z}{L_{\mathrm{wc}}}=0 \tag{6}$$

with boundary conditions as follows

$$-2\lambda_{\mathrm{s}}\cdot\left.\frac{\mathrm{d}T_{\mathrm{s}}}{\mathrm{d}x}\right|_{z=0,L_{\mathrm{monolith}}}=\varepsilon\cdot\sigma\cdot\left(T_{\mathrm{s}}^4-T_{\mathrm{g}}^4\right) \tag{7}$$

where A_{s} is the ratio of the external surface area to the volume of the porous catalyst, A_{cs} is the ratio of the cross sectional area to the volume of the porous catalyst, λ_{s} is the catalyst heat conductivity, ΔH_{r} is the reaction enthalpy, L_{monolith} is the monolith length, ε is the emissivity factor and σ is the Stefan–Boltzmann constant. The discretized forms of eqn

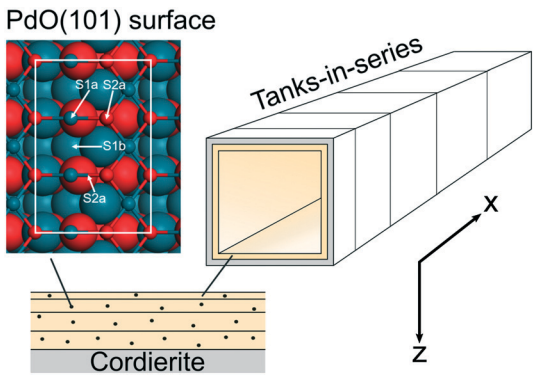

Fig. 1 An illustration of the discretised monolith reactor. The shown numbers of tanks and layers do not correspond to the numbers used in the model. The atomistic model shows a ball and stick model of the PdO(101) surface. Atoms in the top-most layer are visualised with smaller balls. The white line indicates the surface cell. Atomic color code: blue (Pd) and red (O).

This journal is © The Royal Society of Chemistry 2019

This article is licensed under a Creative Commons Attribution 3.0 Unported Licence.

(1)–(7) that were used in the computations were outlined in the study of Azis *et al.*[21]

2.1.1. Calculation of mass and heat transport coefficients. The transport coefficients k_c and h_k between bulk gas and the catalyst surface are determined by Hawthorn's correlations and shown in eqn (8) and (9), respectively.[22] The asymptotic Sherwood and Nusselt numbers are given the value of 2.98:[23]

$$k_{c,i} = \mathrm{Sh}_a \cdot \frac{D_i}{\mathrm{dh}} \cdot \left(1 + \frac{0.095 \cdot \mathrm{Re} \cdot \mathrm{Sc} \cdot \mathrm{dh}}{x}\right)^{0.45} \quad (8)$$

$$h_k = \mathrm{Nu}_a \cdot \frac{\lambda_g}{\mathrm{dh}} \cdot \left(1 + \frac{0.095 \cdot \mathrm{Re} \cdot \mathrm{Pr} \cdot \mathrm{dh}}{x}\right)^{0.45} \quad (9)$$

where D_i is the diffusivity for component i, dh is the open channel diameter, λ_g is the thermal conductivity of the bulk gas and x is the axial position. The value for D_i is corrected according to the Fuller–Schettler–Giddings relationship[24] (eqn (10)):

$$D_i = D_{\mathrm{ref},i} \left(\frac{T_s}{T_{\mathrm{ref}}}\right)^{1.75} \left(\frac{P_{\mathrm{ref}}}{P_{\mathrm{tot}}}\right) \quad (10)$$

where $D_{\mathrm{ref},i}$ is the diffusion coefficient for component i at the reference temperature and pressure. Bulk gas diffusion is assumed to be dominant in the porous catalyst layer and $D_{\mathrm{eff},i}$ is calculated for each component i according to eqn (11)

$$D_{\mathrm{eff},i} = \frac{\varepsilon_p}{\tau} D_i \quad (11)$$

where ε_p is the porosity and τ is the tortuosity of the porous catalyst. The ratio ε_p/τ is set to 0.1, which is within the range of reported ratios.[25,26]

The effectiveness factor is calculated in the axial direction according to eqn (12)

$$\eta = \frac{r_0}{\frac{\int_{z=0}^{z=L_{\mathrm{wc}}} r \mathrm{d}z}{L_{\mathrm{wc}}}} \quad (12)$$

where r_0 denotes the reaction rate under bulk gas conditions. The effectiveness factor includes the external and internal transport resistances.

2.2. Kinetic parameters

The reaction term in eqn (3)–(6) is determined from a first-principles based microkinetic model of methane oxidation on PdO(101). The kinetics is derived from the transition state theory and based on density functional theory using a dual site mechanism.[27] The reaction network considers 43 different surface species and 80 elementary steps. The elementary steps with corresponding kinetic parameters are given in ref. 17 and 27.

2.2.1. Rate coefficients. Adsorption events are described by kinetic gas theory. The rate of adsorption, k_{ads}, is described by eqn (13)

$$k_{\mathrm{ads}} = \frac{S_0^0 S_{\mathrm{dyn}} A_{\mathrm{site}}}{\sqrt{2\pi m_{\mathrm{ads}} k_B T_s}} \cdot \exp\left(\frac{-E_a}{k_B T_s}\right) \quad (13)$$

where A_{site} is the area per adsorption site and set to 10 Å^2, m_{ads} is the mass of the adsorbed molecule, k_B is the Boltzmann constant and E_a is the activation energy. The sticking coefficient is composed of two parts, a sticking coefficient at zero coverage (S_0^0) and a dynamic factor (S_{dyn}). The former is calculated from the transition state theory and originates from the entropy change during the adsorption event. The dynamic part accounts for the fact that a molecule has to approach the active site in a favorable orientation in order to be successfully adsorbed. S_{dyn} is given a fixed value of 10^{-2} for methane and unity for all other molecules. Experimental values for S_{dyn} for CH_4 are reported within the range of 10^{-4}–10^{-1} (ref. 28 and references therein).

The surface reaction rate coefficients, k, are calculated according to the transition state theory[29,30] between the reactant (R) and transition state (TS) as described by eqn (14)

$$k = \frac{k_B T_s}{h} \left(\frac{Q_{\mathrm{TS}}}{\Pi_R Q_R}\right) \cdot \exp\left(-\frac{\Delta E_{\mathrm{TS-R}}}{k_B T_s}\right) \quad (14)$$

where h is Planck's constant, Q is the partition functions of translational, vibrational and rotational motions, which are assumed to be separable, and $\Delta E_{\mathrm{TS-R}}$ is the electronic energy between the reactant and transition state.

The reaction rate for each elementary step is determined by multiplying the rate coefficient, k, with the coverages of the reacting species. Steady state reaction rates and coverages are obtained by solving the set of differential equations shown in eqn (15)

$$\left(\frac{\delta\theta_i(t)}{\delta t} = \sum_i \left(\nu_{ij} r_i\left(\theta_1(t), \ldots, \theta_N(t)\right)\right)\right)_{k,n} \quad (15)$$

where $\theta_i(t)$ is the coverage of surface species i at time t and ν_{ij} is the reaction stoichiometric coefficient for species i and elementary reaction j. Eqn (15) is solved to find the steady state coverages, when the rate of change in coverages equals zero, and reaction rates in each tank k and layer n, using the SciPy Python package.

2.3. Degree of rate control analysis

The method of degree of rate control analysis is used to obtain information about the surface kinetics at varying temperatures and total pressures. The degree of rate control analysis measures the influence of elementary step i on the catalytic

This article is licensed under a Creative Commons Attribution 3.0 Unported Licence.

cycle, while keeping the equilibrium constant fixed for elementary step i.[31,32] The degree of rate control is determined according to eqn (16)

$$\chi_i = \frac{k_i}{r}\left(\frac{\partial r}{\partial k_i}\right)_{K_i} \quad (16)$$

where (χ_i) is the degree of rate control, k_i is the surface reaction rate constant for reaction step i, r is the calculated turn over frequency from the microkinetic model and K_i is the equilibrium constant for reaction step i.

2.4. Reactant conditions and catalyst properties

The methane conversion is simulated through a monolith channel coated with the porous alumina supported palladium catalyst. The feed gas into the monolith is a simulated exhaust gas composed of 1000 vol. ppm CH_4, 10 vol% O_2, 10 vol% H_2O, and 5 vol% CO_2 balanced with inert Ar. A gas hourly space velocity (GHSV) of 53 000 h^{-1} was used for all simulations. The physical properties of the catalyst are taken as reported values of porous alumina. The palladium loading of the catalyst is set to 1 wt% with a palladium dispersion of 25%. The porous catalyst layer is 100 μm thick.

As stated in section 2.1.1, the effective diffusion is taken as 10% of the bulk diffusion. It is common that the Knudsen diffusion is accounted for according to the Bosanquet equation when calculating the effective diffusivity in porous structures where the molecular mean free path and the pore sizes are comparable.[33] However, the Knudsen diffusion is dependent on the porous material and has been discussed, from theoretical and experimental perspectives, to exhibit a relatively low significance on the effective diffusion.[34–40] The molecular diffusion has a dominant effect on the effective diffusivity in a mesoporous structure, while in a microporous structure, the Knudsen diffusion should be considered for a correct estimate of the effective diffusion coefficient. In the present study, the porous structure is assumed to populate meso- and macro-pores, and Knudsen diffusion is hence omitted from the Bosanquet correlation. For comparison, the corresponding conversion when Knudsen diffusion is implemented for a pore size of 10 nm is shown in the ESI.† Steady state performance is simulated for temperatures of 350–500 °C in a step of 5 °C, and at total pressures of 1, 2, 4 and 10 atm. The monolith has a length of 15 mm and a diameter of 12 mm. Further, to study if palladium usage can be more efficient, three additional and different scenarios are included: (1) palladium is unevenly distributed in the axial direction in the monolith, 70% of the total amount is deposited in the first 30% of the monolith length; (2) the catalyst layer thickness is reduced to half (50 μm) and the monolith length is twice its original length (to 30 mm), while keeping the number and distribution of palladium atoms unchanged; and (3) a combination of the two previous scenarios, the catalyst layer is reduced to half and the monolith is doubled in length and 70% of palladium is deposited in the first 30% of the monolith length.

3 Results

3.1. Ignition characteristics of complete methane oxidation

The effect of varying the total pressure on the conversion of methane is shown in Fig. 2. With increased total pressure, the ignition of the reaction proceeds at higher temperature and the conversion at higher temperatures increases. The temperature at which 20% of the methane is converted, T_{20}, is 402, 406, 412 and 421 °C for a total pressure of 1, 2, 4 and 10 atm, respectively. The higher ignition temperature with increasing total pressure correlates with a higher surface coverage of bicarbonates (CO_3H), hydroxyl species (OH) and adsorbed water that adsorb on the S_1(Pd) site which hinders methane adsorption and dissociation. According to the microkinetic model, dissociative methane adsorption occurs on the free S_1(Pd) site as a methyl group and a hydrogen onto a free S_2(O) site, an S_1(Pd)–OH site or an S_1(Pd)–O site, depending on the adsorption mechanism. Further, a more complex effect of the total pressure is observed at intermediate temperatures of 420–445 °C. Here, the methane conversion increases when the total pressure is raised from 1 to 2 and 4 atm but is shown to decrease when the total pressure reaches 10 atm. The observed behaviour is explained in section 4.

3.1.1. Surface coverage dependencies. In Fig. 3, the coverage of CO_3H (solid line), OH (dotted line) and adsorbed H_2O (circles) on the catalyst surface is shown for varying temperatures and total pressures. The reported coverages are weighted averages taken over all tanks in the first layer of the catalyst, *i.e.* at the surface boundary between bulk gas and the catalyst. Two distinct regions are apparent at each examined total pressure. At the lowest temperatures, CO_3H is the most common adsorbate while at higher temperatures adsorbed water and hydroxyl are the dominant species on the catalyst surface. The reported surface species are adsorbed on the S_1(Pd) site and hence hinder methane to adsorb

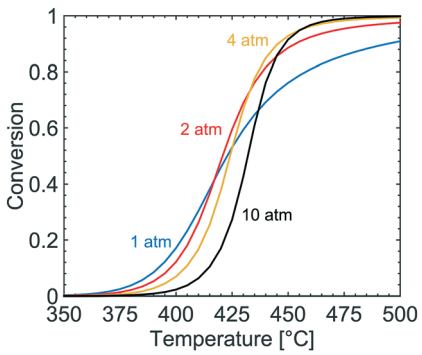

Fig. 2 Simulated methane conversion profiles over the Pd/Al_2O_3 catalyst at total pressures of 1 (blue), 2 (red), 4 (yellow) and 10 (black) atm for gas compositions of 1000 vol. ppm CH_4, 10 vol% O_2, 10 vol% H_2O and 5 vol% CO_2.

This journal is © The Royal Society of Chemistry 2019

This article is licensed under a Creative Commons Attribution 3.0 Unported Licence.

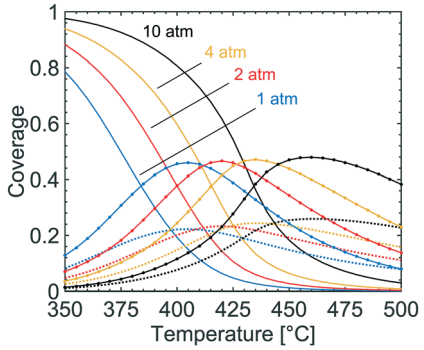

Fig. 3 The coverages of CO_3H (solid lines), OH (dotted lines) and H_2O (circles) at total pressures of 1 (blue), 2 (red), 4 (yellow) and 10 (black) atm for gas compositions of 1000 vol. ppm CH_4, 10 vol% O_2, 10 vol% H_2O and 5 vol% CO_2.

dissociatively. The coverage of free PdO site pairs, *i.e.* an unoccupied S_1(Pd) site next to an unoccupied S_2(O) site, is shown in Fig. 4. As expected, it is observed that the coverage of free PdO site pairs increases with increasing temperature. The low availability of PdO site pairs for dissociative methane adsorption at lower temperatures is explained here by the previous observation of the high probability of finding CO_3H, hydroxyl and water on the S_1(Pd) site, hence also lowering the presence of free site pairs.

3.2. Kinetics of complete methane oxidation for simulated exhaust gas conditions

To obtain the degree of rate control of the elementary steps, the rate of each step was raised by 0.001%. The degree of rate control analysis was performed for the same gas composition as used in the simulations of the conversion profiles, *i.e.* 1000 vol. ppm CH_4, 10 vol% O_2, 10 vol% H_2O and 5 vol% CO_2 balanced with Ar. Fig. 5 shows that methyl decomposition is the step with the highest rate control for all temperatures and total pressures except around 400 °C and 10 atm, where the dissociative methane adsorption is equally important. During methyl decomposition, a hydrogen is transferred to either S_1(Pd)–OH or S_2(O) to form CH_2 and adsorbed water or a surface hydroxyl, respectively. After methyl decomposition, water desorption or dissociative methane adsorption is the step with the highest rate control depending on temperature and total pressure. In general, the rate control of dissociative methane adsorption increases whereas the rate control of water desorption decreases with temperature and total pressure. This is shown in Fig. 5, where at 1 atm the rate control of water desorption is more significant than that of methane adsorption below 475 °C. At 10 atm the rate control of dissociative methane adsorption is more controlling than that of water desorption for all examined temperatures. Since the examined gas composition includes a high concentration of oxygen, the regeneration of oxygen vacancies shows a low rate control while oxygen dissociation, S_1(Pd)–O_2 to 2 S_1(Pd)–O, shows a negative rate control. The latter is explained by slow methane dissociation on S_1–O. Further, surface diffusion of CH_3 and CH_2 from S_1(Pd) to S_2(O) also shows a small positive rate control since a free S_1(Pd) site is formed. Bicarbonate formation has a low rate control despite the fact that CO_2 adsorption blocks the surface sites. The limiting effect of bicarbonate formation is not revealed in the degree of rate control analysis as bicarbonates are not a part of the catalytic cycle. The effect of bicarbonates is instead seen as a negative CO_2 reaction order in Fig. 6, examined at 350 °C for 1 and 10 atm. The reaction order for methane displays a small positive total pressure dependency while the reaction orders of both water and carbon dioxide decrease with increasing total pressures. The observation reinforces the previous results of bicarbonate and water species.

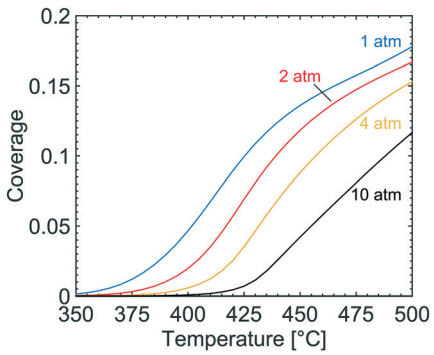

Fig. 4 The coverage of free PdO site pairs, *i.e.* an unoccupied S_1(Pd) site next to an unoccupied S_2(O) site, at total pressures of 1 (blue), 2 (red), 4 (yellow) and 10 (black) atm for gas compositions of 1000 vol. ppm CH_4, 10 vol% O_2, 10 vol% H_2O and 5 vol% CO_2.

3.3. Axial gradients in the monolith channel

Gradients in gas concentration and temperature are evaluated under selected simulation conditions to analyse the complete methane oxidation reaction along the monolith. The selected reaction conditions are at temperatures of 390, 425 and 480 °C, which at a total pressure of 1 atm correspond to methane conversions of 8, 53 and 89%, respectively. The examined total pressures are 1, 2, 4 and 10 atm. The rows in Fig. 7, from top to bottom, show the average reaction rate, bulk gas (diamonds) and catalyst surface temperature (solid line), and the effectiveness factor, respectively, for a total pressure of 1 (blue), 2 (red), 4 (yellow) and 10 (black) atm. The columns in Fig. 7, from left to right, show the results for 390, 425 and 480 °C, respectively. The influence of external and internal mass transport is small and does not induce any significant effects for the examined reaction conditions. When the temperature and the total pressure are increased, the mass transport significance, measured as a comparison of the reaction time constants to the external and internal diffusion time constants, increases but the influence is never strong enough to be reaction rate determining. Further evaluation and discussion of the external and internal mass transport can be found in the ESI.† At 390 °C, the influence of

This article is licensed under a Creative Commons Attribution 3.0 Unported Licence.

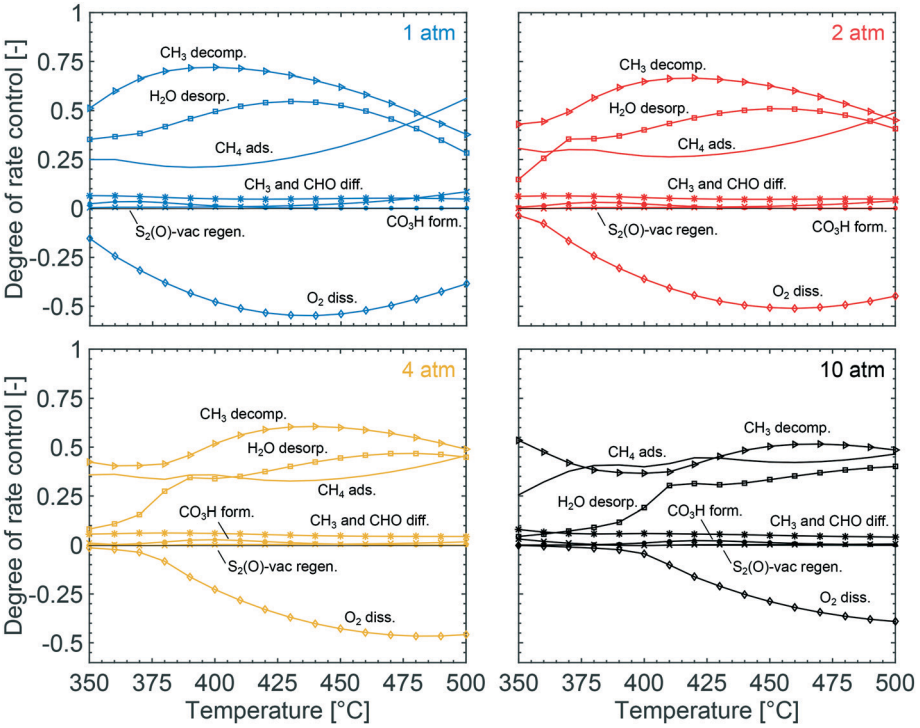

Fig. 5 The degree of rate control for dissociative methane adsorption (solid lines), decomposition of CH_3 (triangles), water desorption (squares), oxygen dissociation over S_1(Pd) (diamonds), S_2-vac regeneration (crosses), methyl and CHO surface diffusion from S_1(Pd) to S_2(O) (stars) and bicarbonate formation (dotted lines) at total pressures of 1 (blue), 2 (red), 4 (yellow) and 10 (black) atm and varying temperatures.

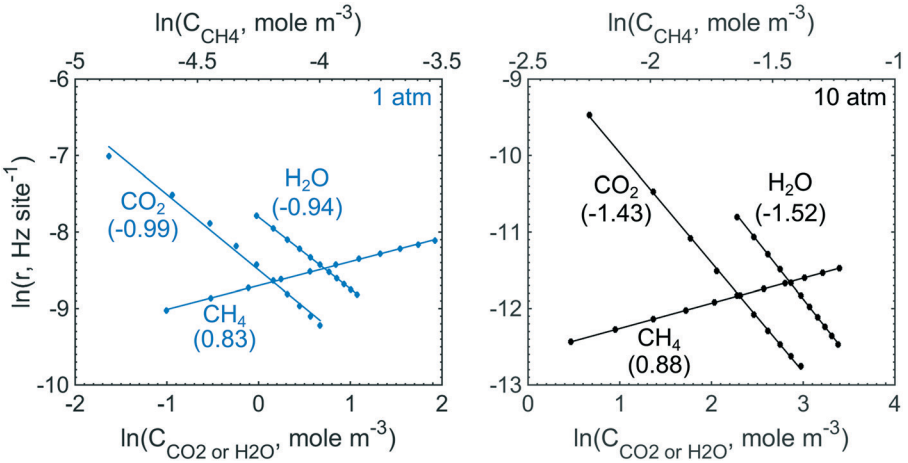

Fig. 6 The reaction orders for methane, water and carbon dioxide at 350 °C and total pressures of 1 (blue) and 10 (black) atm.

mass transport is insignificant for all total pressures due to a slow reaction rate. This is reinforced by an effectiveness factor of ≈1. The average reaction rate is slow at the lowest temperature and thus the axial variations are small and an increased total pressure suppresses the variations even further. At 480 °C and 1 atm, the axial variations are more pronounced due to the higher reaction rate which decreases along the monolith due to the decreasing methane concentration. An axial temperature increase of the catalyst is observed, due to the release of exothermic heat, which in turn has a positive effect on the average reaction rate along the monolith, according to the Arrhenius expression. When the total pressure is increased, temperature dependent total pressure effects are observed. For the simulations at 390 °C, a negative effect is seen on the average reaction rate through the monolith, which leads to the lower conversion in Fig. 2. The reduced reaction rate is explained by the increased coverage of bicarbonates and the reduced availability of active site pairs (Fig. 3 and 4). Further, a reduced temperature increase of the catalyst surface is displayed as a result of the lower reaction rate. For the simulations at 480 °C, the conversion is shown to be enhanced by an increased total pressure, a higher average reaction rate is observed inside the first part of the monolith. The increased average reaction rate is

 This journal is © The Royal Society of Chemistry 2019

This article is licensed under a Creative Commons Attribution 3.0 Unported Licence.

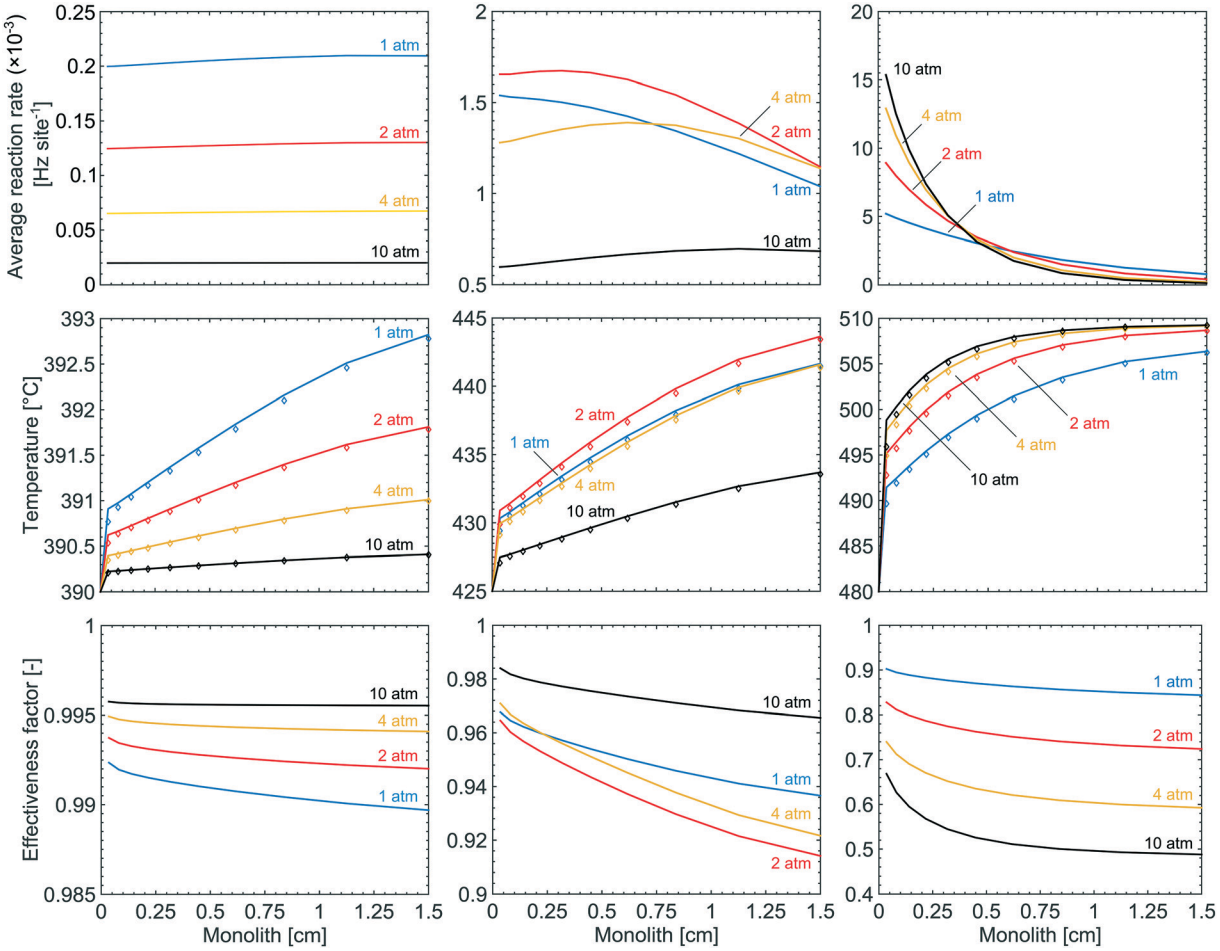

Fig. 7 The axial variations of the average reaction rate, temperature (the solid lines show the catalyst temperature while the diamonds show the gas temperature) and effectiveness factor in a monolith Pd/Al_2O_3 reactor for methane oxidation at total pressures of 1 (blue), 2 (red), 4 (yellow) and 10 (black) atm. Left column: 390 °C. Middle column: 425 °C. Right column: 480 °C.

explained by the availability of active site pairs, where methane can adsorb dissociatively, even at the increased total pressure (Fig. 4). The steep gradient in the average reaction rate along the monolith is explained by the lower methane concentration as the reaction proceeds. When the total pressure is increased the effectiveness factor is significantly reduced as a result of a higher mass transport resistance. The latter is an effect of a higher reaction rate. Interestingly, Fig. 3 shows that for the simulations at 425 °C the conversion increases from 53 to 59% for an increased total pressure from 1 to 2 atm but then drops to 27% when the total pressure is further raised to 10 atm. This effect can be regarded as a transition between the low- and high-temperature effects. Increasing the total pressure from 1 to 2 atm shows that the average reaction rate increases through the entire monolith resulting in the higher conversion. For a total pressure of 4 atm the conversion is the same as for 1 atm but the average reaction rate has leveled out to a steadier value through the monolith. When the total pressure is further increased to 10 atm the average reaction rate decreases due to the increased coverage of hindering species on the catalyst surface, at the cost of a decreased availability of free PdO site pairs (an unoccupied S_1(Pd) site next to an unoccupied S_2(O) site). The bulk gas and catalyst temperatures follow the same trend as for the average reaction rate where an increased reaction rate results in an increased temperature of the catalyst surface, originating from the exothermic heat, and *vice versa*. Since the average reaction rate shows a local maximum in total pressure the effectiveness factor displays a local minimum at 2 atm due to increased mass transport resistance.

3.4. Effects of varied catalyst dimensions and uneven palladium distribution

The effects of redistributing the palladium is evaluated by the three different scenarios described in section 2.4. The methane conversion is shown in Fig. 8 against temperatures above 425 °C for varying total pressures for the three scenarios. None of the three scenarios show an affected methane conversion at temperatures lower than 420 °C but show a positive effect at higher temperatures. In the first scenario the palladium in the catalyst is concentrated to the first part of the monolith and displays a slightly reduced methane conversion at higher temperatures. The largest change is observed at 475 °C and 1 atm

This article is licensed under a Creative Commons Attribution 3.0 Unported Licence.

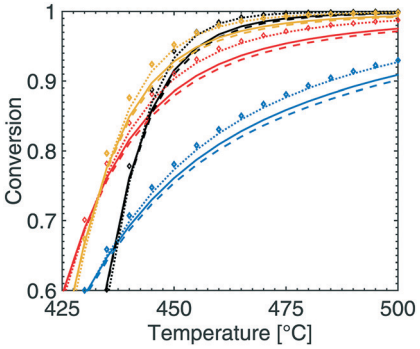

Fig. 8 Methane conversion for the standard scenario (solid lines), concentrated palladium loading to the first part of the monolith (dashed lines), half the catalyst layer thickness and double monolith length (dotted lines) and a combination of the two latter scenarios (diamonds) for temperatures above 425 °C and total pressures of 1 (blue), 2 (red), 4 (yellow) and 10 (black) atm.

where the methane conversion is reduced from 86 to 85%. In the second scenario, where the catalyst layer is reduced to half its original thickness while the monolith length is doubled, an increased methane conversion is observed for all total pressures. The maximum increase is observed at a temperature of 485 °C and 1 atm where the methane conversion increases from 88 to 90%. This maximum increase is shifted down in temperature with increasing total pressure since the original conversion is close to 100% at high temperatures and elevated pressures and hence cannot be improved any further. In other words, there exists an optimal operating temperature point which is between a temperature with a corresponding methane conversion which has the potential to be increased and a higher temperature where full conversion of methane is almost achieved. The maximum is located at 485, 455, 455 and 450 °C for a total pressure of 1, 2, 4 and 10 atm, respectively. The third scenario, which is a combination of the two previous scenarios, shows a similar trend when the catalyst layer is reduced in thickness. It is interesting that the third scenario displays a synergetic effect with the highest potential in enhancing the methane conversion from 86 to 89, at 445 °C and 10 atm. The temperature of the maximum increase in methane conversion decreases with increasing total pressure since the conversion approaches 100% as the total pressure is increased.

4 Discussion

It is shown that the conversion of methane during complete methane oxidation over Pd/Al_2O_3 in a gas composition consisting of 1000 vol. ppm CH_4, 10 vol% O_2, 10 vol% H_2O and 5 vol% CO_2 can be enhanced by increasing the total pressure. The most important effect of the increased total pressure is the enhanced surface coverage of bicarbonates, hydroxyl species and adsorbed water on the active site of the catalyst. The increased coverage of these species is shown to decrease the reaction rate at temperatures below 420 °C. The bicarbonates, hydroxyl species and adsorbed water are, according to the first-principles microkinetics, adsorbed on S_1(Pd) sites and compete with the dissociative methane adsorption, which requires a free PdO site pair (an unoccupied S_1(Pd) next to an unoccupied S_2(O) site) for facile adsorption. When the total pressure is increased, the coverages of these species increase, which results in lower availability of free site pairs at all examined temperatures. The negative total pressure dependence on the reaction rate seen at 390 °C displays the importance of catalyst temperature under the examined gas conditions to maintain a clean catalyst surface. If the total pressure is increased under conditions where the availability of free PdO site pairs is low, a negative effect on the surface reaction rate is to be expected. As shown in Fig. 4 at 390 °C the coverage of free PdO site pairs is low (0.03) and an increased total pressure reduces the possibility for methane to dissociate on the palladium surface close to zero while the coverage of bicarbonates increases from 0.30 to 0.87, see Fig. 3. Since the reaction rate is low the released exothermic heat is not sufficiently high to make a difference to the adsorbate composition. As a result, no positive total pressure effects are seen at 390 °C where bicarbonates, hydroxyl species and adsorbed water are dominant on the catalyst surface. At higher temperatures of above 450 °C (see Fig. 2), a positive effect of increasing the total pressure is observed up to the highest examined total pressure of 10 atm. The result is realised by a high availability of free PdO site pairs in Fig. 4 at all total pressures since thermal energy is supplied to the surface which increases the desorption rate of bicarbionates, hydroxyl species and adsorbed water. The developed multiscale model only considers thermal energy but one may speculate that any energy source or catalyst feature that reduces the coverage of the hindering surface species would yield a similar effect of the total pressure on the catalyst activity. At temperatures between where the negative and positive total pressure dependence are observed, an interesting feature is noticed. At the examined temperature of 425 °C a small increase in total pressure up to 2 atm can enhance the conversion of methane from 53 to 60%. However, if the total pressure is further increased to 10 atm, a significantly lower conversion is seen. The local maximum of methane conversion in total pressure illustrates the interplay between the increased reaction rate and the increased coverage of the hindering surface species bicarbonates, hydroxyl species and adsorbed water. When the total pressure increases from 1 atm to 2 atm the reaction rate is at first enhanced, but above 2 atm the hindering coverage is too high and the reaction rate decreases due to low availability of free active sites. To observe a positive total pressure effect the catalyst surface must not be overwhelmed with the bicarbonates, hydroxyl species and adsorbed water, since the total pressure dependent coverages are the most important factors affecting the reaction rate under the studied reaction conditions. The maximum benefit of increasing the total pressure is achieved at a temperature of 445 °C where the conversion of methane can be increased from 73 to 90% by increasing the total pressure from 1 to 4 atm.

 This journal is © The Royal Society of Chemistry 2019

This article is licensed under a Creative Commons Attribution 3.0 Unported Licence.

The degree of rate control for the intrinsic reaction rate as outlined in section 3.2 shows that the surface kinetics of complete methane oxidation, in simulated exhaust gas compositions, is controlled by the methyl decomposition at lower total pressures while methane adsorption becomes increasingly controlling as the temperature and total pressure are increased. The high gas concentration of H_2O enhances the importance of water desorption, due to a high increased coverage of adsorbed water as seen in Fig. 3, to regenerate a free S_1(Pd) site. Since the elementary step of bicarbonate formation is not a part of the reaction cycle but contributes to the formation of a hindering species in an independent parallel pathway, its degree of rate control is low. The negative effects of carbon dioxide are instead revealed in the analysis of the reaction order. Similarly, a negative reaction order is present for water. At atmospheric total pressure, methane, water and carbon dioxide display a reaction order of 0.83, −0.94 and −0.99, respectively. This is in line with similar work by other groups.[41–43] It should, however, be noted that the experimental conditions differ from the ones used here, but the general explanations follow similar arguments. When the total pressure is increased to 10 atm the reaction order for methane increases slightly, but more noticeable is the stronger negative effect on the reaction orders of water and carbon dioxide.

As shown in Fig. 7, the average reaction rate is significantly enhanced with increasing total pressure in the first part of the monolith. The high reaction rate leads to a higher catalyst temperature, which has a positive feedback effect on the reaction rate. The higher reaction rate leads to steeper axial and radial methane concentration gradients in the monolith which can be understood from the effectiveness factors in Fig. 7. Steeper radial gradients inside the catalyst result in a less efficient use of the active sites furthest into the catalyst layer and hence lower effectiveness factors. The results illustrate the possibilities and constraints when an increased total pressure is available for a synthetic exhaust gas composition. The total pressure can, thus, be used as a design parameter to find new methane abatement systems for vehicle applications. Hence, if a Pd/Al_2O_3 monolith geometry with its desirable flow profile and low mass transport resistances is used for the complete methane oxidation reaction, the conversion of methane can be enhanced by increasing the total pressure if the catalyst temperature is sufficiently high to maintain the necessary availability of free PdO site pairs where the dissociative adsorption of methane occurs. The study also illustrates that a low temperature active methane oxidation catalyst should be resistant to water and carbon dioxide adsorption, in agreement with previous studies.[27,44,45]

The three scenarios shown in section 3.4 demonstrate one way on how this multiscale model can be used to optimise a complex reaction network coupled to mass and heat transport dependencies. Fig. 8 shows that in the first scenario the effect of concentrating the palladium loading to the first part of the monolith (70% of the palladium is distributed into the first 30% of the monolith) only has a minor negative effect on methane conversion. The explanation is found to be an increased mass transport resistance in the palladium dense part of the monolith, due to a higher reaction rate. The increased transport resistance allows more uncombusted methane to slip through into the second part of the monolith with the lower palladium loading. However, the overall effect on methane conversion is low since mass transport has a low impact on the complete methane oxidation reaction under the stated reaction conditions and reactor geometry, see the ESI.† In the second scenario, where the catalyst thickness is reduced and the monolith length is doubled, the methane conversion increases due to a lower impact of mass transport along the entire monolith. This is only observed at higher temperatures since mass transport resistance is insignificant at low temperatures where the reaction rate is low. In the third scenario where the two previous scenarios are combined, a synergetic effect is observed because benefits of lowering the mass transport resistance by a thinner catalyst layer mean a more efficient use of the palladium and at the same time as the length of the palladium dense part of the monolith is made longer. The result is an increased methane conversion not only due to a higher effectiveness factor but also due to a faster temperature increase due to the exothermic heat.

5 Conclusions

A multiscale model based on first-principles surface kinetics shows that the catalyst performance, in terms of methane conversion through a monolith, can be enhanced by increasing the total pressure for a simulated exhaust gas composition from combustion of natural gas. The positive total pressure dependence requires a surface temperature exceeding 420 °C. Below this temperature, a negative total pressure dependence on the methane conversion is displayed. At temperatures of 420–450 °C the conversion exhibits a local maximum in total pressure. The different total pressure dependencies originate from the pressure effects on the coverage of hindering surface species. Bicarbonates, hydroxyl species and adsorbed water originating from gaseous carbon dioxide and water are abundant on the catalyst surface and must desorb or decompose through surface reactions. Otherwise the surface bicarbonates, hydroxyl species and adsorbed water block the active PdO site pairs where methane prefers to adsorb dissociatively. The hindering surface species are adsorbed on the S_1(Pd) sites, according to the first-principle microkinetics, while methane prefers adsorption on free PdO site pairs. The latter is an unoccupied S_1(Pd) site next to an unoccupied S_2(O) site, which are reduced in numbers under low-temperature conditions where the hindering species are abundant on the catalyst surface. The total pressure effects on mass and heat transport are small compared to its effects on surface kinetics. Axial and radial gradients are present at higher temperatures where the reaction rate inside the catalyst is high and the effectiveness factor is lower. Redistributing the palladium in an uneven manner while

reducing the thickness of the catalyst layer is shown to exhibit a synergetic positive effect on methane conversion by a more efficient use of the palladium and catalyst dimensions, and more so at elevated pressures. We have shown here that the total pressure should also be regarded as a possible design parameter to find optimal catalyst geometries and washcoat thicknesses for complete methane oxidation.

Notations

A_c Cross sectional area of the catalyst (m^2)
A_{cs} Ratio of cross sectional area to catalyst volume ($m^2\ m^{-3}$)
A_s Ratio of external surface area to catalyst volume ($m^2\ m^{-3}$)
A_{site} Adsorption site area ($Å^2$)
a Ratio of external surface area to channel volume ($m^2\ m^{-3}$)
C Concentration (mole m^{-3})
C_{site} Active site density (mole kg^{-1})
C_p Bulk gas heat capacity (J $mole^{-1}\ K^{-1}$)
D Bulk diffusivity ($m^2\ s^{-1}$)
D_{eff} Effective diffusivity ($m^2\ s^{-1}$)
D_k Knudsen diffusivity ($m^2\ s^{-1}$)
dh Open channel diameter (m)
E_a Activation energy (eV)
F Molar flow rate (mole s^{-1})
H_r Reaction enthalpy (J $mole^{-1}$)
h Planck's constant (J s)
h_k Heat transport coefficient (W $m^{-2}\ K^{-1}$)
k Rate coefficient for surface reaction (Hz)
k_{ads} Adsorption rate constant (s Pa^{-1})
k_B Boltzmann constant (J K^{-1})
k_c Mass transport coefficient (m s^{-1})
L_{wc} Porous catalyst thickness (m)
m_{ads} Mass of adsorbed molecule (kg)
m_{cat} Mass of porous catalyst (kg)
Nu_a Asymptotic Nusselt number
P Pressure (Pa)
Pr Prandlt number
Q Partition function
Re Reynolds number
r Reaction rate/turnover frequency (Hz $site^{-1}$)
Sc Schmidt number
S_0^0 Sticking coefficient at zero coverage
S_{dyn} Dynamic sticking coefficient
Sh_a Asymptotic Sherwood number
T Temperature (K)
x Axial direction
y Mole fraction
z Radial direction

Greek letters

ε Emissivity factor
ε_p Porosity
η Effectiveness factor
Θ Coverage
λ Thermal conductivity (W $m^{-1}\ K^{-1}$)
ν Stoichiometric coefficient
ρ Density (kg m^{-3})
σ Stefan–Boltzmann constant (W $m^{-2}\ K^{-4}$)

Subscripts

cat Catalyst
g Gas
i Component index
j Elementary reaction index
k Tank index
n Catalyst layer index
R Reactant state
r Reaction
ref Reference
s Solid
TS Transition state
tot Total
wc Washcoat

Conflicts of interest

There are no conflicts to declare.

Acknowledgements

This work has been performed within the Competence Centre for Catalysis, which is hosted by Chalmers University of Technology and financially supported by the Swedish Energy Agency and the member companies AB Volvo, ECAPS AB, Johnson Matthey AB, Preem AB, Scania CV AB, Umicore Denmark ApS and Volvo Car Corporation AB. Additional support from the Swedish Research Council is acknowledged as well as computational resources at C3SE (Göteborg) *via* an SNIC grant.

References

1 BP, *Statistical Review of World Energy*, 2018.
2 IEA, *Natural Gas information: Overview*, 2017.
3 M. Gambino, R. Cericola, P. Corbo and S. Iannaccone, *J. Eng. Gas Turbines Power*, 1993, **115**, 747–749.
4 S. Achinas, V. Achinas and G. J. W. Euverink, *Engineering*, 2017, **3**, 299–307.
5 Q. Zhang, J. Hu and D.-J. Lee, *Renewable Energy*, 2016, **98**, 108–119.
6 U.S Department of Energy, *Renewable Natural Gas (Biomethane) Production*, https://www.afdc.energy.gov/fuels/natural_gas_renewable.html, Accessed on 2018-07-10.
7 H. Li, D. Mehmood, E. Thorin and Z. Yu, *Energy Procedia*, 2017, **105**, 1172–1177.
8 Environmental Protection Agency, *Overview of Greenhouse Gases*, https://www.epa.gov/ghgemissions/overview-greenhouse-gases, Accessed on 2018-07-10.
9 D. Ciuparu, M. R. Lyubovsky, E. Altman, L. D. Pfefferle and A. Datye, *Catal. Rev.: Sci. Eng.*, 2002, **44**, 593–649.

This article is licensed under a Creative Commons Attribution 3.0 Unported Licence.

This journal is © The Royal Society of Chemistry 2019

This article is licensed under a Creative Commons Attribution 3.0 Unported Licence.

10 Z. Li and G. B. Hoflund, *J. Nat. Gas Chem.*, 2003, **12**, 153–160.
11 P. Gélin and M. Primet, *Appl. Catal., B*, 2002, **39**, 1–37.
12 P. A. Carlsson, E. Fridell and M. Skoglundh, *Catal. Lett.*, 2007, **115**, 1–7.
13 N. M. Martin, M. Van den Bossche, A. Hellman, H. Grönbeck, C. Hakanoglu, J. Gustafson, S. Blomberg, N. Johansson, Z. Liu, S. Axnanda, J. F. Weaver and E. Lundgren, *ACS Catal.*, 2014, **4**, 3330–3334.
14 A. Hellman, A. Resta, N. M. Martin, J. Gustafson, A. Trinchero, P.-A. Carlsson, O. Balmes, R. Felici, R. van Rijn, J. W. M. Frenken, J. N. Andersen, E. Lundgren and H. Grönbeck, *J. Phys. Chem. Lett.*, 2012, **3**, 678–682.
15 A. Antony, A. Asthagiri and J. F. Weaver, *J. Chem. Phys.*, 2013, **139**, 104702.
16 A. Trinchero, A. Hellman and H. Grönbeck, *Phys. Status Solidi RRL*, 2014, **8**, 605–609.
17 C.-R. Florén, M. Van den Bossche, D. Creaser, H. Grönbeck, P.-A. Carlsson, H. Korpi and M. Skoglundh, *Catal. Sci. Technol.*, 2018, **8**, 508–520.
18 C. Ericson, B. Westerberg and I. Odenbrand, *SAE World Congress & Exhibition*, 2008.
19 D. Creaser, X. Karatzas, B. Lundberg, L. J. Pettersson and J. Dawody, *Appl. Catal., A*, 2011, **404**, 129–140.
20 J. B. Anderson, *Chem. Eng. Sci.*, 1963, **18**, 147–148.
21 M. M. Azis, H. Härelind and D. Creaser, *Chem. Eng. J.*, 2013, **221**, 382–397.
22 R. Hawthorne, *AIChE Symp. Ser.*, 1974, **70**, 428.
23 T. Enrico and F. Pio, *AIChE J.*, 1992, **38**, 201–210.
24 E. N. Fuller, P. D. Schettler and J. C. Giddings, *Ind. Eng. Chem. Res.*, 1966, **58**, 18–27.
25 K. C. Metaxas and N. G. Papayannakos, *Chem. Eng. J.*, 2008, **140**, 352–357.
26 A. Şahin, E. Alp, D. Eserci and H. C. Cabbar, *Chem. Eng. Commun.*, 2017, **204**, 1129–1142.
27 M. Van den Bossche and H. Grönbeck, *J. Am. Chem. Soc.*, 2015, **137**, 12035–12044.
28 H. Abbott and I. Harrison, *J. Catal.*, 2008, **254**, 27–38.
29 M. G. Evans and M. Polanyi, *Trans. Faraday Soc.*, 1935, **31**, 875–894.
30 H. Eyring, *J. Chem. Phys.*, 1935, **3**, 107–115.
31 C. T. Campbell, *ACS Catal.*, 2017, **7**, 2770–2779.
32 M. Jørgensen and H. Grönbeck, *Catal. Sci. Technol.*, 2017, **7**, 4034–4040.
33 W. G. Pollard and R. D. Present, *Phys. Rev.*, 1948, **73**, 762–774.
34 V. Novák, F. Štěpánek, P. Kočí, M. Marek and M. Kubíček, *Chem. Eng. Sci.*, 2010, **65**, 2352–2360.
35 V. Novák, P. Kočí, M. Marek, F. Štěpánek, P. Blanco-García and G. Jones, *Catal. Today*, 2012, **188**, 62–69.
36 V. Novák, P. Kočí, T. Gregor, J. S. Choi, F. Štěpánek and M. Marek, *Catal. Today*, 2013, **216**, 142–149.
37 P. Kočí, F. Štěpánek, M. Kubíček and M. Marek, *Chem. Eng. Sci.*, 2007, **62**, 5380–5385.
38 P. Kočí, V. Novák, F. Štěpánek, M. Marek and M. Kubíček, *Chem. Eng. Sci.*, 2010, **65**, 412–419.
39 M. Dudák, V. Novák, P. Kočí, M. Marek, P. Blanco-García and G. Jones, *Appl. Catal., A*, 2014, **150-151**, 446–458.
40 B. Lundberg, J. Sjöblom, Å Johansson, B. Westerberg and D. Creaser, *Appl. Catal., A*, 2016, **191**, 116–129.
41 R. Monteiro, D. Zemlyanov, J. Storey and F. Ribeiro, *J. Catal.*, 2001, **199**, 291–301.
42 F. H. Ribeiro, M. Chow and R. A. Dalla Betta, *J. Catal.*, 1994, **146**, 537–544.
43 G. Zhu, J. Han, D. Y. Zemlyanov and F. H. Ribeiro, *J. Chem. Phys.*, 2005, **109**, 2331–2337.
44 R. Burch, F. Urbano and P. Loader, *Appl. Catal., A*, 1995, **123**, 173–184.
45 R. Gholami, M. Alyani and K. Smith, *Deactivation of Pd Catalysts by Water during Low Temperature Methane Oxidation Relevant to Natural Gas Vehicle Converters*, 2015, vol. 5, pp. 561–594.